POLITECNICO DI TORINO
Repository ISTITUZIONALE

Computational replication of the patient-specific stenting procedure for coronary artery bifurcations: From OCT and CT imaging to structural and hemodynamics analyses

Original
Computational replication of the patient-specific stenting procedure for coronary artery bifurcations: From OCT and CT imaging to structural and hemodynamics analyses / Chiastra, Claudio; Wu, Wei; Dickerhoff, Benjamin; Aleiou, Ali; Dubini, Gabriele; Otake, Hiromasa; Migliavacca, Francesco; Ladisa John, F. - In: JOURNAL OF BIOMECHANICS. - ISSN 0021-9290. - ELETTRONICO. - 49:11(2016), pp. 2102-2111. [10.1016/j.jbiomech.2015.11.024]

Availability:
This version is available at: 11583/2770475 since: 2019-11-28T16:19:03Z

Publisher:
Elsevier

Published
DOI:10.1016/j.jbiomech.2015.11.024

Terms of use:

This article is made available under terms and conditions as specified in the corresponding bibliographic description in the repository

Publisher copyright
Elsevier postprint/Author's Accepted Manuscript

© 2016. This manuscript version is made available under the CC-BY-NC-ND 4.0 license
http://creativecommons.org/licenses/by-nc-nd/4.0/.The final authenticated version is available online at:
http://dx.doi.org/10.1016/j.jbiomech.2015.11.024

(Article begins on next page)

25 April 2024

Accepted manuscript at http://dx.doi.org/10.1016/j.jbiomech.2015.11.024

Computational replication of the patient-specific stenting procedure for coronary artery bifurcations: from OCT and CT imaging to structural and hemodynamics analyses

Claudio Chiastra[1,2], Wei Wu[1], Benjamin Dickerhoff[3], Ali Aleiou[3], Gabriele Dubini[1], Hiromasa Otake[4], Francesco Migliavacca[1], John F. LaDisa Jr.[3,5]

1 Laboratory of Biological Structure Mechanics (LaBS), Department of Chemistry, Materials and Chemical Engineering "Giulio Natta", Politecnico di Milano, Milan, Italy

2 Department of Biomedical Engineering, Thoraxcenter, Erasmus University Medical Center, Rotterdam, The Netherlands

3 Department of Biomedical Engineering, Marquette University, Milwaukee, WI, USA

4 Kobe University Graduate School of Medicine, Kobe, Japan

5 Department of Medicine, Division of Cardiovascular Medicine, Medical College of Wisconsin, Milwaukee, WI, USA

Address for correspondence:
John F. LaDisa Jr.
Marquette University
Department of Biomedical Engineering
1637 West Wisconsin Ave.
Milwaukee, WI 53233
United States

Phone: +1-414-288-6739
E-mail: john.ladisa@marquette.edu

Post-print version

ABSTRACT

The optimal stenting technique for coronary artery bifurcations is still debated. With additional advances computational simulations can soon be used to compare stent designs or strategies based on verified structural and hemodynamics results in order to identify the optimal solution for each individual's anatomy. In this study, patient-specific simulations of stent deployment were performed for 2 cases to replicate the complete procedure conducted by interventional cardiologists. Subsequent computational fluid dynamics (CFD) analyses were conducted to quantify hemodynamics quantities linked to restenosis.

Patient-specific pre-operative models of coronary bifurcations were reconstructed from CT angiography and optical coherence tomography (OCT). Plaque location and composition were also determined from OCT and assigned to models, and structural simulations were performed in Abaqus. Artery geometries after virtual stent expansion of Xience Prime or Nobori stents created in SolidWorks were compared to post-operative geometry from OCT and CT before being extracted and used for CFD simulations in SimVascular. Inflow boundary conditions were based on body surface area, and downstream vascular resistances and capacitances were applied at branches to mimic physiology.

Quantitative comparison between the post-stent and reconstructed geometries revealed a maximum area difference of 20.4%. Adverse hemodynamics were more pronounced for thicker Nobori stents in both patients. These findings verify structural analyses of stent expansion, introduce a workflow to combine software packages for solid and fluid mechanics analysis, and underscore important stent design features from prior idealized studies. The proposed approach may ultimately be useful in determining an optimal choice of stent and position for each patient.

Post-print version

Keywords: mathematical model, finite element analysis, computational fluid dynamics, coronary bifurcation, stent

1. INTRODUCTION

The treatment of complex coronary lesions such as bifurcation lesions remains a challenge in interventional cardiology because of lower success rates and higher restenosis rates as compared to non-complex lesions (Lassen et al., 2014). Since the introduction of drug eluting stents in 2004, restenosis rate after stent implantation have fallen below 10% in several randomized clinical trials (Dangas et al., 2010). However, this rate increases when coronary bifurcation lesions are treated (Lemos et al., 2004; Mauri et al., 2008; Zahn et al., 2005).

The optimal stenting technique for treating diseased coronary bifurcations is still debated without a consensus among interventional cardiologists (Lassen et al., 2014). Indeed, the post-operative follow-up is influenced by different factors such as stent design (Morton et al., 2004; Timmins et al., 2011, 2008), the use of one or two stents (Katritsis et al., 2009; Zhang et al., 2009), plaque morphology and composition (Timmins et al., 2008), arterial injury caused by stent deployment (Kornowski et al., 1998; Schwartz et al., 1992), and adverse hemodynamics induced by the stent struts protruding inside the lumen (Foin et al., 2014). A number of studies proved that neointima thickening (NT), which can lead to in-stent restenosis, is related to increased wall stress post-stenting (Timmins et al., 2011) and to altered local fluid dynamics (e.g. low and oscillating wall shear stress; WSS) provoked by the stent presence within the coronary artery (LaDisa Jr. et al., 2005; Malek et al., 1999).

In this context, virtual simulations of patient-specific coronary bifurcation stenting can be used to compare the effect of different stent designs or stenting strategies on structural and fluid dynamics results in order to identify the optimal solution for each individual's anatomy (Migliavacca et al., 2015). In several previous studies (Chiastra et al., 2013; Ellwein et al., 2011; Gundert et al., 2011; Morlacchi et al., 2013; Mortier et al., 2015) patient-specific structural and fluid dynamic simulations were conducted. However, the post-operative geometry obtained after virtual stent deployment was rarely compared with the *in vivo* post-operative images (Morlacchi et al., 2013). Moreover, when performed, this comparison is often qualitative and based only on computed tomography (CT) and angiography data. The use of optical coherence tomography (OCT) images allows better model verification, because of its high spatial resolution compared to CT and angiography (Farooq et al., 2009; Ferrante et al., 2013).

In this study patient-specific simulations of stent deployment are performed to replicate the complete procedure followed by clinicians to treat coronary bifurcations. OCT and CT images are used to reconstruct the 3D models of the coronary bifurcations. The reliability of structural finite-element analyses (FEA) in predicting post-operative geometric outcomes is evaluated. Subsequent computational fluid dynamics (CFD) analyses are conducted to quantify the influence of local

Post-print version

hemodynamics variables (e.g. indices of WSS). Different stent designs and stent positioning within the patient-specific models are studied to explore potential post-operative scenarios.

2. MATERIALS AND METHODS

2.1 Imaging and reconstruction of artery morphology and composition

Accurate reconstruction of artery geometry is critical to the patient-specific modeling process, and depends on imaging resolution. This study used a hybrid approach of CT angiography and OCT to reconstruct artery geometry within the stented region by mathematically determining the location of the OCT imaging wire during image acquisition (Ellwein et al., 2011). These method combines conventional and invasive high-resolution imaging modalities (**Fig.1A**). We refer to the use of CT and OCT data with this approach as *Hybrid OC-CT* (see details below).

This investigation was approved by the ethics committees of all participating institutions. Informed consent was obtained for the use of data in this study. Coronary angiography, CT and OCT imaging were performed before (i.e. pre-PCI) and immediately after stenting (i.e. post-stent) as previously reported (Otake et al., 2009). OCT images were acquired and quantified as discussed elsewhere (Ellwein et al., 2011; Nakazato et al., 2015).

Separate pre-PCI and post-stenting lumen models were created for two patients (namely, Cases 1 and 2). Case 1 consisted of a left anterior descending/first diagonal (LAD/D1) bifurcation of a 70-year-old female while Case 2 is a left circumflex artery (LCX) with two branches of a 73-year-old male. Both cases had a stenosis >80% in the main artery by angiography. Pre-PCI lumen models were used to simulate local deformations caused by stenting from FEA (see details below). The post-stenting models were created to validate the accuracy of deformations from FEA. For both lumen models (i.e. pre-PCI and post-stenting), high resolution OCT segments were registered within the region of interest using *Hybrid OC-CT* (Ellwein et al., 2011). Briefly, OCT images were processed to isolate lumen contours in Matlab (MathWorks Inc., Natick, MA, USA). The wire pullback pathway (**Fig.1A**) was determined by minimizing total bending energy within the lumen volume delineated by CT. Lumen segments from OCT were then registered on the wire pathway using landmarks where possible. Remaining lumen segments were then positioned longitudinally according to OCT image spacing. All lumen segments were then oriented orthogonal to the wire pathway and rotated such that their centroids aligned with the artery centerline. The aligned and oriented lumen segments were loaded into SimVascular (simtk.org) for lofting and blending, thus obtaining lumen geometries (**Fig.1A**).

OCT data did not allow for measurement of wall thickness because of its reduced tissue penetration (Waksman et al., 2013). To create external arterial wall surfaces (**Fig.1B**),

Post-Print version

circumferential cross-sections orthogonal to artery centerlines were lofted for regions devoid of plaque. The external wall diameters were set to comply with the internal diameter and physiological wall thickness of healthy coronary branches (Morlacchi et al., 2013). The arterial wall was meshed with ~100,000 eight-node cubic elements with reduced integration using ICEM CFD (ANSYS Inc., Canonsburg, PA, USA) (**Fig.2A**). An isotropic hyperplastic constitutive model was implemented to describe the arterial wall material properties (Morlacchi et al., 2013). This model is based on experimental values measured from media layer specimens of human coronary arteries (Holzapfel et al., 2005).

Since the exact radial plaque position within the arterial wall could not be deduced by the patient images, a previously developed method for plaque identification (Morlacchi et al., 2013) was applied and extended (**Fig.2A**). First, a centerline was identified from the external wall surface. Second, the distance between this centerline and each element of the arterial wall was calculated in the radial direction. Lastly, a healthy radius was assumed based on angiography inspection of non-atherosclerotic locations. All elements with a distance less than the healthy radius (**Fig.2A**, black arrows) were considered as plaque.

A different composition was then assigned to each region of plaque. To achieve this, a trained interventional cardiologist manually delineated different plaque regions on the longitudinal section view of the collection of OCT images (**Fig.2B-C**). In Case 1 the majority of the plaque was classified as soft (**Fig.2B**). In Case 2 the plaque was mainly stiff (i.e. fibrous plaque) with a small region of soft material (i.e. fibrous and lipid plaque) close to the proximal side branch (**Fig.2C**). Soft and stiff plaques were modeled using an isotropic hyperelastic law based on experimental data (Loree et al., 1994) with ideal plasticity to simulate rupture at the experimental tensile stress values (~400kPa).

2.2 Stent and balloon models

The commercially available Xience Prime (Abbott Laboratories, Abbott Park, IL, USA) and Nobori (Terumo, Somerset, NJ, USA) DES were considered in this study. The two stents are characterized by a different strut thickness (Xience Prime=81μm; Nobori=125μm). Geometries were created using SolidWorks (Dassault Systèmes SolidWorks Corp., Waltham, MA, USA). Both stents are fabricated from a cobalt-chromium alloy that can be described by a von Mises-Hill plasticity model with isotropic hardening. The following material properties were assigned to the stent models during FEA: Young modulus (233 GPa), Poisson coefficient (0.35), yield stress (414 MPa), ultimate stress (933 MPa), and deformation at break (44.5%). The geometries were discretized with a highly

Post-print version

regular hexahedral mesh of ~120,000 reduced integration cubic elements using HyperMesh software package (Altair Engineering, Troy, MI, USA).

Geometric models of angioplasty and stent delivery balloons were created in their crimped configuration using SolidWorks. The balloon thickness was 0.025 mm. The polymeric material of the balloons was described using a linear elastic isotropic model with a Young modulus of 1.45 GPa and a Poisson coefficient of 0.3. The balloon models were discretized with ~25,000 reduced integration membrane elements.

2.3 Structural simulations of stent deployment

The following virtual stent expansion simulations were performed in the coronary bifurcation models to replicate the real stenting procedure performed by the interventional cardiologists who treated the cases featured (**Fig.3**):

1) Angioplasty: a balloon was inserted at the site of the atherosclerotic lesion and then inflated to open the narrowed coronary artery. 2.5x18 mm and 3.5x18 mm balloons were used for Cases 1 and 2, respectively.
2) Provisional side branch stenting technique (PSB): first, a stent in its crimped state was positioned in the main branch at the narrowing. Second, the stent was expanded by balloon inflation. Last, the balloon was deflated and the stent remained in place, holding the artery open. 2.5x18 mm Xience Prime and 3.5x18 mm Nobori stents were implanted in Cases 1 and 2, respectively.

Stent expansions were conducted in Abaqus/Explicit (Dassault Systèmes Simulia Corp., Providence, RI, USA) as a quasi-static process as discussed in detail elsewhere (Morlacchi et al., 2013, 2011).

To investigate the biomechanical influence of different stent designs and position, additional scenarios were also examined. Cases 1 and 2 were used to evaluate hemodynamic performance by comparing CFD results from Xience Prime and the Nobori stents. Case 2 was also used to evaluate the importance of stent positioning on the post-operative geometry obtained after virtual stent deployment relative to that from post-stent patient images via *Hybrid OC-CT*. Specifically, the Nobori stent was virtually implanted in three different positions by moving the stent distally relative to the first diagonal branch.

2.4 CFD simulations

Lumen and arterial wall deformations from FEA were extracted for CFD. Briefly, a NASTRAN file exported from ICEM CFD was loaded into ParaView (Kitware Inc., Clifton Park, NY, USA) where the surface was extracted and saved as a VTK multiblock file. A discrete solid model was then

Post-print version

created from this surface file using SimVascular. Faces were renamed to delineate between those of the stent and artery wall for use in assigning edge sizes to mesh elements. Meshing parameters were iteratively adjusted until the meshing procedure was successful at writing out a mesh of sufficient density to resolve local flow features, while working within the computational limits of the local CPU (HP Z420 E5-1620 3.6 GHz workstations with 16GB RAM).

Boundary conditions for CFD were determined from patient-specific anthropometric data as discussed elsewhere (Ellwein et al., 2011). Briefly, using cardiac output, blood flow through the artery undergoing stenting was determined assuming the coronary arteries receive 5% of the cardiac output, and the right and left coronary arteries receive 16% and 84%, respectively (Ellwein et al., 2011; Leaman et al., 1981). An inflow waveform (LaDisa Jr. et al., 2002) was then scaled to match the mean blood flow, and introduced as a time-varying Womersley velocity profile. Blood was assumed to be a Newtonian fluid with a viscosity and constant density of 4 cP and 1.06 gm/cm^3, respectively. WSS was assumed to be equal in the main vessel and side branches (Ellwein et al., 2011; Williams et al., 2010). A three-element Windkessel representation was applied at each outlet to replicate the physiological influence of the arterial tree distal to the arteries in the computational model (Ellwein et al., 2011; Williams et al., 2010).

CFD simulations were run using an in house stabilized finite element solver with commercial linear solver component LESLIB (Altair Engineering) to solve the time-dependent Navier-Stokes equations. Standard convergence criteria were employed and simulations were run until the outlet pressure and flow were periodic.

2.5 Analysis of results

The open-source software PyFormex (www.nongnu.org/pyformex/) was used to quantify the distance between lumen surfaces of the post-stent geometry obtained after virtual stent deployment and *Hybrid OC-CT*. The two geometries were manually registered using the position of the side branches as a reference. The area of the geometry obtained after virtual stent deployment with a distance greater than 0.25 mm (i.e. twice the strut thickness of the Nobori stent) was then calculated.

Malapposed struts (defined as struts not in contact or within 0.1 mm of the lumen surface) were identified (Iannaccone et al., 2014). The percent area of malapposed struts with respect to the total area of the abluminal stent surface was calculated.

Indices of WSS previously linked to NT were also determined. Time-averaged WSS (TAWSS) and oscillatory shear index (OSI) were computed over the last cardiac cycle as in previous studies (He and Ku, 1996; Tang et al., 2006) and visualized using ParaView. It has been shown that low

Post-print version

TAWSS (<0.4 Pa) and high temporal oscillations quantified by OSI (>0.1) are associated with NT (LaDisa Jr. et al., 2005; Malek et al., 1999; Wentzel et al., 2008), therefore the artery surface exposed to values outside these limits was used to quantify the impact of the implanted stent.

3. RESULTS

The reliability of FEA for virtual stent deployment was first verified. FEA took ~24 hours on one node of a cluster (two quad-core Intel Xeon E5620 2.40 GHz with 3 GB RAM and INFINIBAND Mellanox interconnections). **Figure 4** shows superimposition of the post-operative lumen geometry obtained after virtual stent expansion and that from *Hybrid OC-CT*. A good qualitative agreement between the two geometries can be observed for both cases. Regions of the post-operative geometries obtained after virtual stent expansion with a distance >0.25 mm relative to those reconstructed from *Hybrid OC-CT* are highlighted in red. Percent differences in area were 14.8% and 20.4% for Cases 1 and 2, respectively.

Malapposed struts are highlighted in red in **Figs.5-6** for both cases, and the percent area of malapposed struts is reported in **Table 1** for both Xience Prime and Nobori stents. For Case 1, malapposed struts are only present in the bifurcation ostium (**Fig.5**). For Case 2, malapposed struts are localized at the bifurcation ostia and also at the proximal part of the stent (**Fig.6**). The percent area of malapposed struts was reduced from ~4.9% to ~1.3% by moving the Nobori stent distally to the first branch from Position A to Position C (**Table 1, Fig.6**). The Xience Prime showed a lower percentage of malapposition than Nobori implanted in the implanted position (i.e. Position B), likely due to its different stent design impacting interaction with components of the arterial wall.

CFD analysis was subsequently performed to quantify post-stenting results between different stent designs. CFD run times averaged ~15 hours per simulation (range 8-26 hours) using 56 cores of an Intel Nehalem cluster with 3 GB/core of RAM.

Distributions of TAWSS for Case 1 are shown in **Fig.7**. The patient for this case was implanted with a 2.5x18 mm Xience Prime stent (**Fig.7A**). Virtual implantation of a 2.5x18 mm Nobori stent is also shown for comparison (**Fig.7B**). Portions of the artery lumen exposed to adverse TAWSS previously implicated in NT (i.e. < 0.4 Pa) are also shown in the figure. The area of low TAWSS was more pronounced for the Nobori stent as compared to the Xience Prime stent that was actually implanted (6.80% vs 4.07%, **Table 2**). Straightening of the artery caused skewing of the velocity profile toward the surface nearest the bifurcation, and resulted in a pronounced area of low TAWSS on the opposite surface within the proximal portion of the stent. A second focal region of low TAWSS was found directly opposite the bifurcation. The degree to which this region extended circumferentially was influenced by the stent implanted, and the orientation of struts within this

Post-print version

region. Sites of low TAWSS were more pronounced around struts of the Nobori stent due to their greater thickness. This prevented re-establishing of local near-wall velocity patterns as was observed distal to the bifurcation for the Xience Prime stent. Distributions of OSI are shown in **Fig.8**. Overall artery morphology in the proximal stented region and the bifurcation also contributed to elevated OSI in these regions, but differences in the area exposed to OSI > 0.1 were more modest than for TAWSS (3.55% vs 3.70% for the Xience Prime and Nobori stents, respectively, **Table 2**).

Distributions of TAWSS for Case 2 are shown in **Fig 9**. The patient for this case was implanted with a 3.5x18 mm Nobori stent (**Fig.9A**) and virtual implantation of a 3.5x18 mm Xience Prime stent is also shown for comparison (**Fig.9B**). Areas of low TAWSS were localized to the entrance region of both stents where there was a sudden expansion in diameter, as well as downstream from an adjacent region of residual plaque and malapposition in the Nobori stent. The area of low TAWSS in Case 2 was also more pronounced for the Nobori stent as compared to the Xience Prime stent (27.1% vs 22.5%, Table 2). The regions of sudden expansion and downstream of the residual plaque within the stent also contributed to elevated OSI in these regions (**Fig.10**), and differences in the area exposed to OSI>0.1 were more pronounced than for Case 1 (8.15% vs 6.02% for the Nobori and Xience Prime, respectively, **Table 2**).

4. DISCUSSION

The use of computer models for predicting and interpreting outcomes related to the treatment of coronary artery bifurcation stenting is gaining popularity, and garining an increasing level of interest (Migliavacca et al., 2015; Mortier et al., 2015, 2010). This is likely due in large part to a number of papers in recent years showing how patient-specific data can be used to precisely reproduce the anatomy of a coronary bifurcation, which can then be subjected to virtual bench testing of stents. These computational studies have generated striking agreement with experimental results suggesting they can be useful and powerful tools that shed additional light on aspects of interest to interventional cardiologists (Chiastra et al., 2015). This approach is particularly useful for the quantification of stent malapposition or indices of WSS in stented regions that are not immediately measurable during a procedure. With this in mind, the current investigation underscores the use of patient-specific FEA with subsequent CFD modeling as a means of predicting post-operative scenarios without necessarily having to physical deploy a stent. The main findings of this work are related to verifying FEA of stent expansion, successful integration of a workflow combining multiple software packages for solid and fluid mechanics analysis, and an alignment of patient-specific CFD results generated from this workflow with stent design features that have been shown to be important in idealized studies to date.

Post-print version

In completing the objective above, the current work acheives several notable 'firsts'. In contrast to using an idealized artery or single imaging modality for reconstruction before FEA, the pre-PCI and post-stenting artery geometries here were created using *Hybrid OC-CT*, which allows for reconstruction at 15 μm resolution. The pre-PCI reconstruction was used as the starting point for FEA, and the post-stenting reconstruction was used to scrutinize the accuracy of its subsequent local deformations, which represents another unique aspect of the current investigation. The use of a sequential approach (i.e. from FEA to CFD analyses) allowed us to take also into account the local deformation of the artery lumen due to stent expansion. As previously demonstrated (Martin et al., 2014; Morlacchi et al., 2011), local hemodynamics are very sensitive to the stented geometry and a sequential approach can provide a more accurate replication of the local hemodynamic environment.

The post-stent geometries obtained after virtual expansion were qualitatevely in good agreement with those from patient images. Quantitative comparison between the post-stent geometries resulted in a maximum area difference of 20.4% (Case 2). We believe this is a very promising result. The manual registration process followed in this study is believed to have resulted in overestimation of differences in geometry obtained after virtual stent deployment relative to the geometry reconstructed from patient images. An optimization process could be implented for registration of the post-stent geometries in order to minimize the areas with distance higher than 0.25 mm.

We also presented a workflow that, while accounting for all the steps conducted by an interventional cardiologist, can systematically be used to quantify the relative contributions of geometrical factors (e.g. strut malapposition) and biomechanical stimuli. The consideration of factors from a solid mechanics (e.g. local deformation) and fluid mechanics (e.g. WSS) perspective is unique, but also very important since both have been implicated in restenosis and markers of late stent thrombosis. The approach presented here blends some of the most common and well documented software packages from both the commercial and open source domains. Although atypical, this approach allows us to leveage the best features from mutiple software packages and provides a starting point for other researcher to do the same.

The current work also paves the way for the use of simulations in larger trials to predictively evaluate the optimal stent for a given patient and/or assess their risk for suboptimal clinical outcomes rooted in biomechanics after coronary artery DES implantation. For example, the notion of being able to select the optimal stent for a given patient was investigated for both cases by comparing the Xience Prime and Nobori stents in terms of malapposion, TAWSS, and OSI results. The best stent position was evaluted virtually by implanting the Nobori stent in three different positions. The percentage of malapposed struts was reduced by moving the stent distally to the first

Post-Print version

branch. The case with the stent in its implanted position (Position B) showed results bounded by the two extreme positions. The patient-specific cases presented here also confirm conclusions from prior idealized studies regarding stent design characteristics and their effect on adverse WSS distributions. Stent geometry has been shown to affect the distribution of WSS, and, in turn, affect NT (LaDisa Jr. et al., 2005). Gundert et al. (Gundert et al., 2013) reviewed a hierarchy of factors that can result in adverse WSS distributions by virtually implanting various stents into idealized coronary arteries. The hierarchy includes strut thickness that was drastically different between the two stents used in the current investigation, stent-to-lumen area ratio, angle of struts relative to the primary direction of blood flow, and the arrangement of connector elements (Gundert et al., 2012). However, it is concevible that not all patient-specific CFD simulations conduted from FEA will adhere to this hierarchy of design features elucidated by theoretical stented CFD models. Exclusions may include stents with similar strut thicknesses, or patients with a more complex plaque distribution creating a heterogeneity in material properties within the stented region.

The advancements shown in this work are perfectly timed as ~150 key opinion leaders from academia, industry and cardiology recently expressed their willingness to adopt a new way of thinking that includes the possibility of simulating interventions using patient-specific data (Stankovic et al., 2013). Unfortunately enthusiasm is tempered by the fact that translation of virtual patient-specific computational modeling to the clinic is dependent on the time needed to obtain the results, as well as to their reliability. To complete the full procedure applied here (artery reconstruction to FEA and CFD), ~3 days are required with the available computational resources. Further advancements to speed up and automate the procedure are therefore required.

Although this study shows promising results, some limitations are present. The plaque identification process might be improved with more tissue testing and expedited by implementing a semi-automatic algorithm for delinating the location and composition of plaque from OCT data (Celi and Berti, 2014; Celi et al., 2013). Limitations of the CFD simulations are related to the boundary conditions imposed, and neglecting movement of the arterial wall after stent implantation. Closed-loop, lumped-parameter networks, initially developed to model single ventricle physiology, were recently applied to the coronary arteries (Sankaran et al., 2012). Implementation of these tools would better replicate relationships between local flow and global circulatory dynamics (Bove et al., 2007; Corsini et al., 2011; Kim et al., 2010). The rigid-wall assumption implemented here appears adequate when the aim of the study is the analysis of near-wall hemodynamic quantities (Chiastra et al., 2014) within the stent since implantation typically renders most of the artery rigid (LaDisa Jr. et al., 2002).

Post-Print version

5. CONCLUSIONS

The methodology described here to virtually simulate stent implantation is reliable by taking into account intrinsic errors and assumptions due to image reconstruction and numerical modeling. Furthermore, the proposed workflow (from FEA to CFD analyses) may provide useful information for pre-interventional planning by choosing the optimal stent type and position for each individual's anatomy.

6. ACKNOWLEDGEMENTS

This work was supported in part by National Science Foundation (NSF) awards OCI-0923037 and CBET-0521602. Claudio Chiastra is partially supported by the ERC starting grant (310457, BioCCora). Wei Wu is supported by the Politecnico di Milano International Fellowship (PIF) program. The authors acknowledge Laura Ellwein PhD (Assistant Professor of Mathematics at Virginia Commonwealth University, Richmond, VA, USA) for implementation of the *Hybrid OC-CT* approach.

7. CONFLICT OF INTEREST

The authors have no conflicts of interest to declare.

8. REFERENCES

Bove, E.L., de Leval, M.R., Migliavacca, F., Balossino, R., Dubini, G., 2007. Toward optimal hemodynamics: computer modeling of the Fontan circuit. Pediatr. Cardiol. 28, 477–81.

Celi, S., Berti, S., 2014. In-vivo segmentation and quantification of coronary lesions by optical coherence tomography images for a lesion type definition and stenosis grading. Med. Image Anal. 18, 1157–1168.

Celi, S., Vaghetti, M., Palmieri, C., Berti, S., 2013. Superficial coronary calcium analysis by OCT: Looking forward an imaging algorithm for an automatic 3D quantification. Int. J. Cardiol. 168, 2958–2960.

Post-print version

Chiastra, C., Grundeken, M.J., Wu, W., Serruys, P.W., de Winter, R.J., Dubini, G., Wykrzykowska, J.J., Migliavacca, F., 2015. First report on free expansion simulations of a dedicated bifurcation stent mounted on a stepped balloon. EuroIntervention 10, e1–3.

Chiastra, C., Morlacchi, S., Gallo, D., Morbiducci, U., Cárdenes, R., Larrabide, I., Migliavacca, F., 2013. Computational fluid dynamic simulations of image-based stented coronary bifurcation models. J. R. Soc. Interface 10, 20130193.

Corsini, C., Cosentino, D., Pennati, G., Dubini, G., Hsia, T.Y., Migliavacca, F., 2011. Multiscale models of the hybrid palliation for hypoplastic left heart syndrome. J. Biomech. 44, 767–770.

Dangas, G.D., Claessen, B.E., Caixeta, A., Sanidas, E. a., Mintz, G.S., Mehran, R., 2010. In-stent restenosis in the drug-eluting stent era. J. Am. Coll. Cardiol. 56, 1897–1907.

Ellwein, L.M., Otake, H., Gundert, T.J., Koo, B.-K., Shinke, T., Honda, Y., Shite, J., LaDisa, J.F., 2011. Optical Coherence Tomography for Patient-specific 3D Artery Reconstruction and Evaluation of Wall Shear Stress in a Left Circumflex Coronary Artery. Cardiovasc. Eng. Technol. 2, 212–227.

Farooq, M.U., Khasnis, A., Majid, A., Kassab, M.Y., 2009. The role of optical coherence tomography in vascular medicine. Vasc. Med. 14, 63–71.

Ferrante, G., Presbitero, P., Whitbourn, R., Barlis, P., 2013. Current applications of optical coherence tomography for coronary intervention. Int. J. Cardiol. 165, 7–16.

Foin, N., Gutiérrez-Chico, J.L., Nakatani, S., Torii, R., Bourantas, C. V., Sen, S., Nijjer, S., Petraco, R., Kousera, C., Ghione, M., Onuma, Y., Garcia-Garcia, H.M., Francis, D.P., Wong, P., Di Mario, C., Davies, J.E., Serruys, P.W., 2014. Incomplete stent apposition causes high shear flow disturbances and delay in neointimal coverage as a function of strut to wall detachment distance implications for the management of incomplete stent apposition. Circ. Cardiovasc. Interv. 7, 180–189.

Gundert, T.J., Dholakia, R.J., McMahon, D., LaDisa, J.F., 2013. Computational fluid dynamics evaluation of equivalency in hemodynamic alterations between Driver, Integrity, and similar stents implanted into an idealized coronary artery. J. Med. Device. 7, 11004.

Gundert, T.J., Marsden, A.L., Yang, W., Marks, D.S., LaDisa Jr., J.F., 2012. Identification of hemodynamically optimal coronary stent designs based on vessel caliber. IEEE Trans Biomed Eng 59, 1992–2002.

Gundert, T.J., Shadden, S.C., Williams, A.R., Koo, B.K., Feinstein, J. a., Ladisa, J.F., 2011. A rapid and computationally inexpensive method to virtually implant current and next-generation stents into subject-specific computational fluid dynamics models. Ann. Biomed. Eng. 39, 1423–1437.

He, X., Ku, D.N., 1996. Pulsatile flow in the human left coronary artery bifurcation: average conditions. J. Biomech. Eng 118.

Holzapfel, G.A., Sommer, G., Gasser, C.T., Regitnig, P., 2005. Determination of layer-specific mechanical properties of human coronary arteries with nonatherosclerotic intimal thickening and related constitutive modeling. Am J Physiol Hear. Circ Physiol 289, H2048–58.

Post-print version

Iannaccone, F., De Bock, S., De Beule, M., Vermassen, F., Van Herzeele, I., Verdonck, P., Segers, P., Verhegghe, B., 2014. Feasibility of a priori numerical assessment of plaque scaffolding after carotid artery stenting in clinical routine: proof of concept. Int. J. Artif. Organs 37, 928–939.

Katritsis, G.D., Siontis, G.C.M., Ioannidis, J.P. a, 2009. Double versus single stenting for coronary bifurcation lesions a meta-analysis. Circ. Cardiovasc. Interv. 2, 409–415.

Kim, H.J., Vignon-Clementel, I.E., Figueroa, C. a., Jansen, K.E., Taylor, C. a., 2010. Developing computational methods for three-dimensional finite element simulations of coronary blood flow. Finite Elem. Anal. Des. 46, 514–525.

Kornowski, R., Hong, M.K., Tio, F.O., Bramwell, O., Wu, H., Leon, M.B., 1998. In-stent restenosis: Contributions of inflammatory responses and arterial injury to neointimal hyperplasia. J. Am. Coll. Cardiol. 31, 224–230.

LaDisa Jr., J.F., Hettrick, D.A., Olson, L.E., Guler, I., Gross, E.R., Kress, T.T., Kersten, J.R., Warltier, D.C., Pagel, P.S., 2002. Stent implantation alters coronary artery hemodynamics and wall shear stress during maximal vasodilation. J Appl Physiol 93, 1939–1946.

LaDisa Jr., J.F., Olson, L.E., Molthen, R.C., Hettrick, D.A., Pratt, P.F., Hardel, M.D., Kersten, J.R., Warltier, D.C., Pagel, P.S., 2005. Alterations in wall shear stress predict sites of neointimal hyperplasia after stent implantation in rabbit iliac arteries. Am J Physiol Hear. Circ Physiol 288, H2465–75.

Lassen, J.F., Holm, N.R., Stankovic, G., 2014. Percutaneous coronary intervention for coronary bifurcation disease : consensus from the first 10 years of the European Bifurcation Club meetings 545–560.

Leaman, D.M., Brower, R.W., Meester, G.T., Serruys, P., van den Brand, M., 1981. Coronary artery atherosclerosis: severity of the disease, severity of angina pectoris and compromised left ventricular function. Circulation 63, 285–299.

Lemos, P.A., Serruys, P.W., van Domburg, R.T., Saia, F., Arampatzis, C.A., Hoye, A., Degertekin, M., Tanabe, K., Daemen, J., Liu, T.K.K., McFadden, E., Sianos, G., Hofma, S.H., Smits, P.C., van der Giessen, W.J., de Feyter, P.J., 2004. Unrestricted utilization of sirolimus-eluting stents compared with conventional bare stent implantation in the “real world”: the Rapamycin-Eluting Stent Evaluated At Rotterdam Cardiology Hospital (RESEARCH) registry. Circulation 109, 190–5.

Loree, H.M., Grodzinsky, A.J., Park, S.Y., Gibson, L.J., Lee, R.T., 1994. Static circumferential tangential modulus of human atherosclerotic tissue. J Biomech 27, 195–204.

Malek, a M., Alper, S.L., Izumo, S., 1999. Hemodynamic shear stress and its role in atherosclerosis. JAMA 282, 2035–2042.

Martin, D.M., Murphy, E. a., Boyle, F.J., 2014. Computational fluid dynamics analysis of balloon-expandable coronary stents: Influence of stent and vessel deformation. Med. Eng. Phys. 36, 1047–1056.

Post-print version

Mauri, L., Silbaugh, T.S., Wolf, R.E., Zelevinsky, K., Lovett, A., Zhou, Z., Resnic, F.S., Normand, S.-L.T., 2008. Long-term clinical outcomes after drug-eluting and bare-metal stenting in Massachusetts. Circulation 118, 1817–27.

Migliavacca, F., Chiastra, C., Chatzizisis, Y.S., Dubini, G., 2015. Virtual bench testing to study coronary bifurcation stenting. EuroIntervention 11 Suppl V, V31–V34.

Morlacchi, S., Chiastra, C., Gastaldi, D., Giancarlo, P., Dubini, G., Migliavacca, F., 2011. Sequential structural and fluid Dynamic numerical simulations of a stented bifurcated coronary artery. J. Biomech. Eng. 133, 121010.

Morlacchi, S., Colleoni, S.G., Cárdenes, R., Chiastra, C., Diez, J.L., Larrabide, I., Migliavacca, F., 2013. Patient-specific simulations of stenting procedures in coronary bifurcations: two clinical cases. Med. Eng. Phys. 35, 1272–81.

Mortier, P., De Beule, M., Dubini, G., Hikichi, Y., Murasato, Y., Ormiston, J.A., 2010. Coronary bifurcation stenting: insights from in vitro and virtual bench testing. EuroIntervention 6 Suppl J, J53–60.

Mortier, P., De Beule, M., Segers, P., Verdonck, P., Verhegghe, B., 2011. Virtual bench testing of new generation coronary stents. EuroIntervention 7, 369–376.

Mortier, P., Wentzel, J.J., De Santis, G., Chiastra, C., Migliavacca, F., De Beule, M., Louvard, Y., Dubini, G., 2015. Patient-specific computer modelling of coronary bifurcation stenting: the John Doe programme. EuroIntervention 11 Suppl V, V35–V39.

Morton, A.C., Crossman, D., Gunn, J., 2004. The influence of physical stent parameters upon restenosis. Pathol. Biol. 52, 196–205.

Nakazato, R., Otake, H., Konishi, A., Iwasaki, M., Koo, B.-K., Fukuya, H., Shinke, T., Hirata, K.-I., Leipsic, J., Berman, D.S., Min, J.K., 2015. Atherosclerotic plaque characterization by CT angiography for identification of high-risk coronary artery lesions: a comparison to optical coherence tomography. Eur. Heart J. Cardiovasc. Imaging 16, 373–9.

Otake, H., Shite, J., Ako, J., Shinke, T., Tanino, Y., Ogasawara, D., Sawada, T., Miyoshi, N., Kato, H., Koo, B.K., Honda, Y., Fitzgerald, P.J., Hirata, K., 2009. Local determinants of thrombus formation following sirolimus-eluting stent implantation assessed by optical coherence tomography. JACC Cardiovasc Interv 2, 459–466.

Sankaran, S., Esmaily Moghadam, M., Kahn, A.M., Tseng, E.E., Guccione, J.M., Marsden, A.L., 2012. Patient-specific multiscale modeling of blood flow for coronary artery bypass graft surgery. Ann Biomed Eng 40, 2228–2242.

Schwartz, R.S., Huber, K.C., Murphy, J.G., Edwards, W.D., Camrud, a R., Vlietstra, R.E., Holmes, D.R., 1992. Restenosis and the proportional neointimal response to coronary artery injury: results in a porcine model. J. Am. Coll. Cardiol. 19, 267–274.

Stankovic, G., Lefevre, T., Chieffo, A., Hildick-Smith, D., Lassen, J.F., Pan, M., Darremont, O., Albiero, R., Ferenc, M., Finet, G., Adriaenssens, T., Koo, B.K., Burzotta, F., Louvard, Y., 2013. Consensus from the 7th European Bifurcation Club meeting. EuroIntervention 9, 36–45.

Post-print version

Tang, B.T., Cheng, C.P., Draney, M.T., Wilson, N.M., Tsao, P.S., Herfkens, R.J., Taylor, C.A., 2006. Abdominal aortic hemodynamics in young healthy adults at rest and during lower limb exercise: quantification using image-based computer modeling. Am J Physiol Hear. Circ Physiol 291, H668–76.

Timmins, L.H., Meyer, C. a, Moreno, M.R., Moore, J.E., 2008. Effects of stent design and atherosclerotic plaque composition on arterial wall biomechanics. J. Endovasc. Ther. 15, 643–654.

Timmins, L.H., Miller, M.W., Clubb, F.J., Moore, J.E., 2011. Increased artery wall stress post-stenting leads to greater intimal thickening. Lab. Invest. 91, 955–967.

Waksman, R., Kitabata, H., Prati, F., Albertucci, M., Mintz, G.S., 2013. Intravascular ultrasound versus optical coherence tomography guidance. J. Am. Coll. Cardiol. 62, S32–S40.

Wentzel, J.J., Gijsen, F.J.H., Schuurbiers, J.C.H., van der Steen, A.F.W., Serruys, P.W., 2008. The influence of shear stress on in-stent restenosis and thrombosis. EuroIntervention 4 Suppl C, C27–C32.

Williams, A.R., Koo, B.-K., Gundert, T.J., Fitzgerald, P.J., LaDisa, J.F., 2010. Local hemodynamic changes caused by main branch stent implantation and subsequent virtual side branch balloon angioplasty in a representative coronary bifurcation. J. Appl. Physiol. 109, 532–40.

Zahn, R., Hamm, C.W., Schneider, S., Zeymer, U., Nienaber, C.A., Richardt, G., Kelm, M., Levenson, B., Bonzel, T., Tebbe, U., Sabin, G., Senges, J., 2005. Incidence and predictors of target vessel revascularization and clinical event rates of the sirolimus-eluting coronary stent (results from the prospective multicenter German Cypher Stent Registry). Am. J. Cardiol. 95, 1302–8.

Zhang, F., Dong, L., Ge, J., 2009. Simple versus complex stenting strategy for coronary artery bifurcation lesions in the drug-eluting stent era: a meta-analysis of randomised trials. Heart 95, 1676–81.

Post-print version

TABLE CAPTIONS

Table 1 – Malapposition for all investigated cases.

Table 2 – Indices of wall shear stress (WSS) including time-averaged wall shear stress (TAWSS) and oscillatory shear index (OSI). These indices were compared between the implanted stent for Cases 1 and 2 (Xience Prime and Nobori, respectively) and virtual implantation of the second stent.

Post-print version

FIGURE CAPTIONS

Figure 1 – Creation of a patient-specific coronary artery bifurcation model using Case 1 as an example. A) *Hybrid OC-CT* method to obtain the 3D lumen geometry (Ellwein et al., 2011): (top) detection of lumen contours, (center) registration of the detected contours orthogonal to the imaging wire pathway, (bottom) final 3D lumen geometry, which was obtained by lofting lumen contours after registration. The center panel also shows differences between the imaging wire pathway (black) and the lumen centerline (grey). B) 3D solid model of the lumen and vessel wall.

Figure 2 – Plaque modeling. A) Plaque identification process (Morlacchi et al., 2013) using Case 2 as an example. The distance between each grid node and the centerline of the external wall is computed. The elements are characterized by assuming a distance less than the physiological lumen radius represents regions of plaque. B-C) Assignment of plaque composition, which is based on the information given by optical coherence tomography (OCT) images, for Cases 1 and 2, respectively.

Figure 3 – Main steps of the stenting procedure that was followed for Cases 1 (left) and 2 (right): A) insertion of the angioplasty balloon; B) expansion of the angioplasty balloon; C) insertion of the stent crimped on a balloon; D) stent expansion; E) final geometric configuration after stent recoil.

Figure 4 – Comparison between the post-stenting geometry reconstructed from patient images (grey) and the geometry obtained after virtual stent deployment (blue) for Cases 1 (left) and 2 (right). Regions of the geometry obtained after virtual stent deployment that are greater than 0.25 mm from the geometry reconstructed from patient images are shown in red. Comparison was only performed in the stented region. Two views are shown for clarity as indicated by differences in the flow direction in the top vs bottom images.

Figure 5 – Quantification of stent malapposition for Case 1: A) Xience Prime stent; B) Nobori stent. Malapposed struts are shown in red.

Figure 6 – Quantification of stent malapposition for Case 2. A-C) Nobori stent in the three positions investigated; D) Xience Prime stent. Malapposed struts are shown in red.

Figure 7 – Time-averaged wall shear stress (TAWSS) distributions for Case 1. Differences in TAWSS previously linked to neointimal thickness are shown in the figure and quantified in Table 2 by comparing CFD results from the implanted Xience Prime stent (A) vs the virtually-implanted

Post-print version

Nobori stent (B). Two views are shown for clarity as indicated by differences in the flow direction in the left vs right images. The full range of TAWSS values is shown for both stents in each view. The lumen area exposed to the TAWSS < 0.4 Pa (see legend) is also isolated for both stents in each view.

Figure 8 – Oscillatory shear index (OSI) distributions for Case 1. Differences in OSI are shown in the figure and quantified in Table 2 by comparing CFD results from the implanted Xience Prime stent (A) vs the virtually-implanted Nobori stent (B). Two views are shown for clarity as indicated by differences in the flow direction in the left vs right images.

Figure 9 – Time-Averaged Wall Shear Stress (TAWSS) distributions for Case 2. Differences in TAWSS previously linked to neointimal thickness are shown in the figure and quantified in Table 2 by comparing CFD results from the implanted Nobori stent (A) vs the virtually-implanted Xience Prime stent (B). Two views are shown for clarity as indicated by differences in the flow direction in the left vs right images. The full range of TAWSS values is shown for both stents in each view. The lumen area exposed to the TAWSS < 0.4 Pa (see legend) is also isolated for both stents in each view.

Figure 10 – Oscillatory Shear Index (OSI) distributions for Case 2. Differences in OSI are shown in the figure and quantified in Table 2 by comparing CFD results from the implanted Nobori stent (A) vs the virtually-implanted Xience Prime stent (B). Two views are shown for clarity as indicated by differences in the flow direction in the left vs right images.

Post-print version

TABLES

Table 1 – Malapposition for all investigated cases.

Case	Stent	Malapposition [perc. area with distance > 0.1 mm]
1	Xience Prime (*Implanted*)	0.90 %
1	Nobori	1.53 %
2	Nobori (pos. A)	4.92 %
2	Nobori (pos. B - *Implanted*)	2.35 %
2	Nobori (pos. C)	1.32 %
2	Xience Prime (pos. B)	0.95 %

Table 2 – Indices of wall shear stress (WSS) including time-averaged wall shear stress (TAWSS) and oscillatory shear index (OSI). These indices were compared between the implanted stent for Cases 1 and 2 (Xience Prime and Nobori, respectively) and virtual implantation of the second stent.

Case	Stent	TAWSS [perc. area TAWSS < 0.4 Pa]	OSI [perc. area with OSI > 0.1]
1	Xience Prime (*Implanted*)	4.07 %	3.55%
1	Nobori	6.80 %	3.70 %
2	Nobori (*Implanted*)	27.1 %	8.15 %
2	Xience Prime	22.5 %	6.02 %

Post-print version

FIGURES

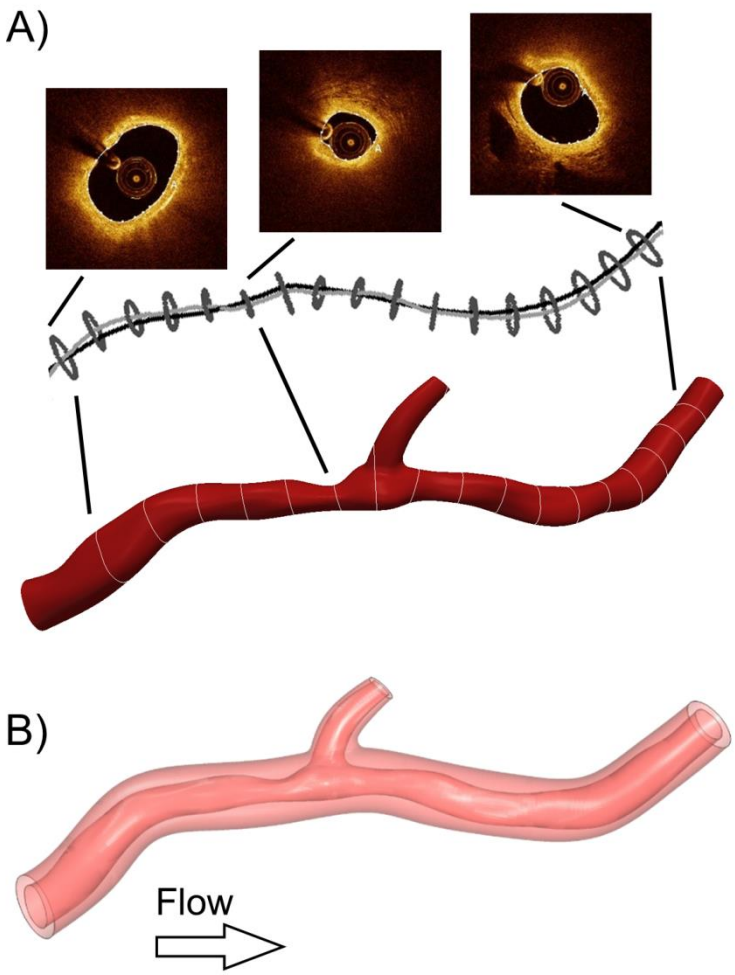

Figure 1 – Creation of a patient-specific coronary artery bifurcation model using Case 1 as an example. A) *Hybrid OC-CT* method to obtain the 3D lumen geometry (Ellwein et al., 2011): (top) detection of lumen contours, (center) registration of the detected contours orthogonal to the imaging wire pathway, (bottom) final 3D lumen geometry, which was obtained by lofting lumen contours after registration. The center panel also shows differences between the imaging wire pathway (black) and the lumen centerline (grey). B) 3D solid model of the lumen and vessel wall.

Post-print version

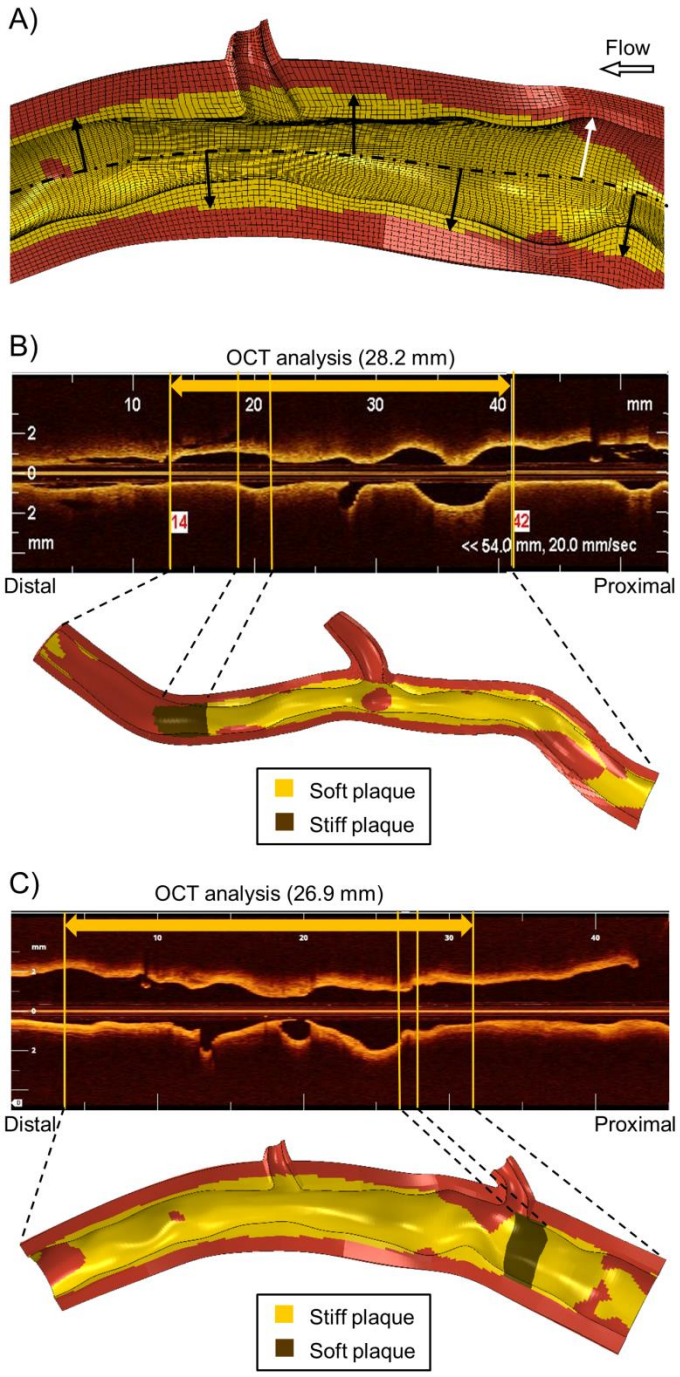

Figure 2 – Plaque modeling. A) Plaque identification process (Morlacchi et al., 2013) using Case 2 as an example. The distance between each grid node and the centerline of the external wall is computed. The elements are characterized by assuming a distance less than the physiological lumen radius represents regions of plaque. B-C) Assignment of plaque composition, which is based on the information given by optical coherence tomography (OCT) images, for Cases 1 and 2, respectively.

Post-print version

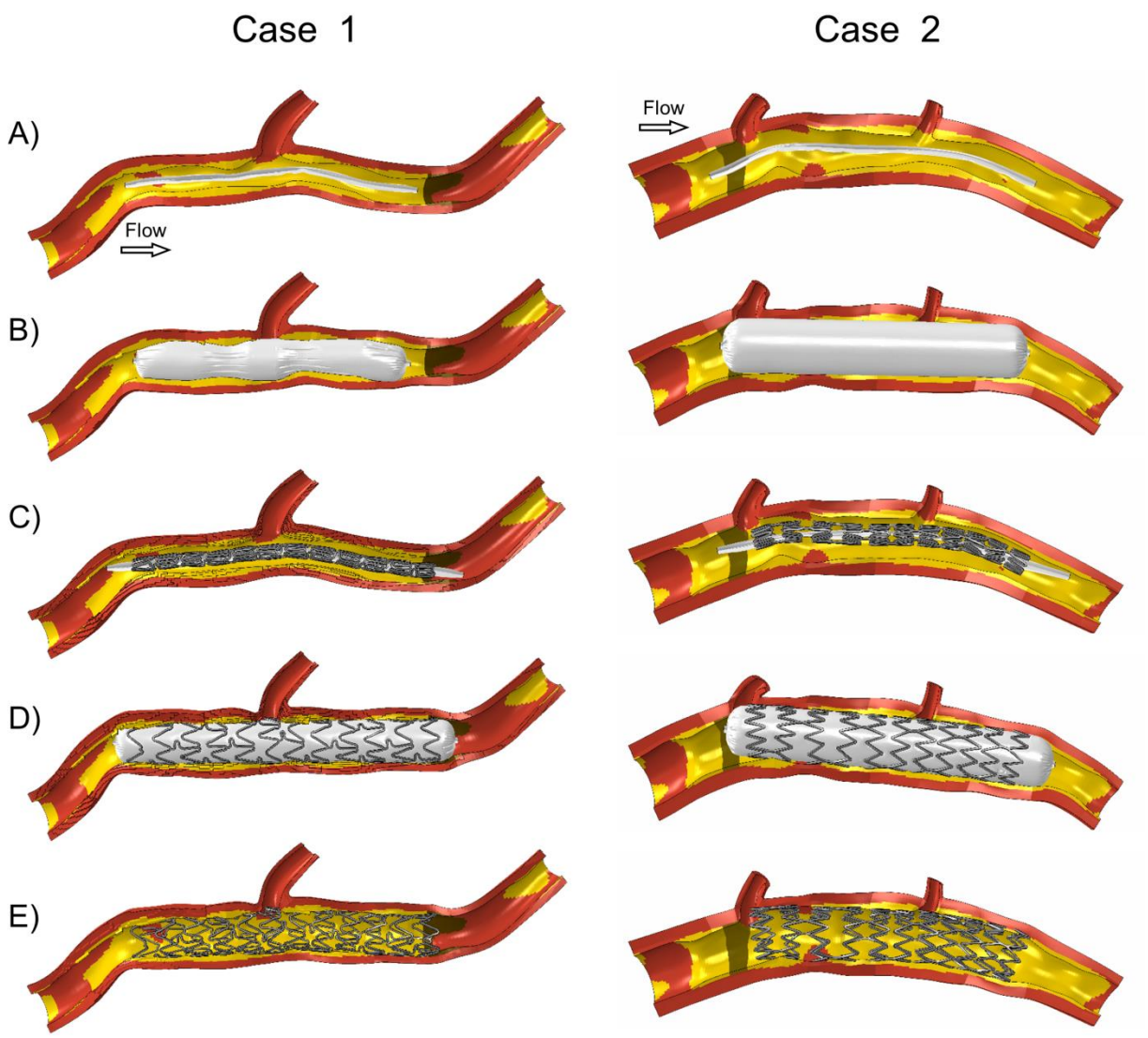

Figure 3 – Main steps of the stenting procedure that was followed for Cases 1 (left) and 2 (right): A) insertion of the angioplasty balloon; B) expansion of the angioplasty balloon; C) insertion of the stent crimped on a balloon; D) stent expansion; E) final geometric configuration after stent recoil.

Post-p

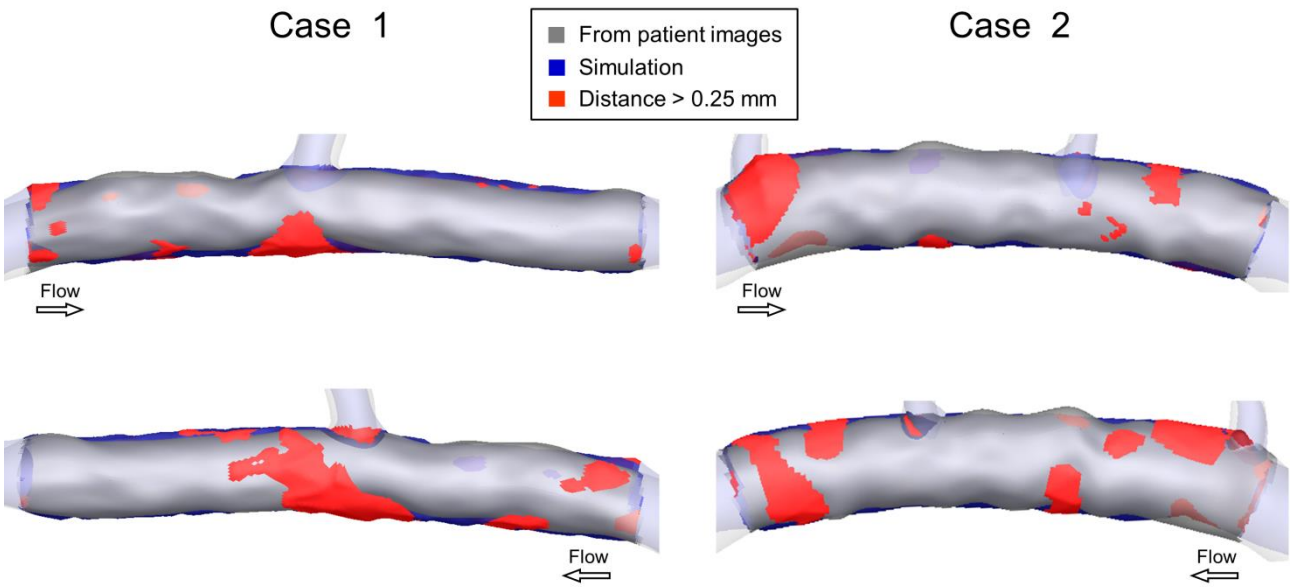

Figure 4 – Comparison between the post-stenting geometry reconstructed from patient images (grey) and the geometry obtained after virtual stent deployment (blue) for Cases 1 (left) and 2 (right). Regions of the geometry obtained after virtual stent deployment that are greater than 0.25 mm from the geometry reconstructed from patient images are shown in red. Comparison was only performed in the stented region. Two views are shown for clarity as indicated by differences in the flow direction in the top vs bottom images.

Post-print version

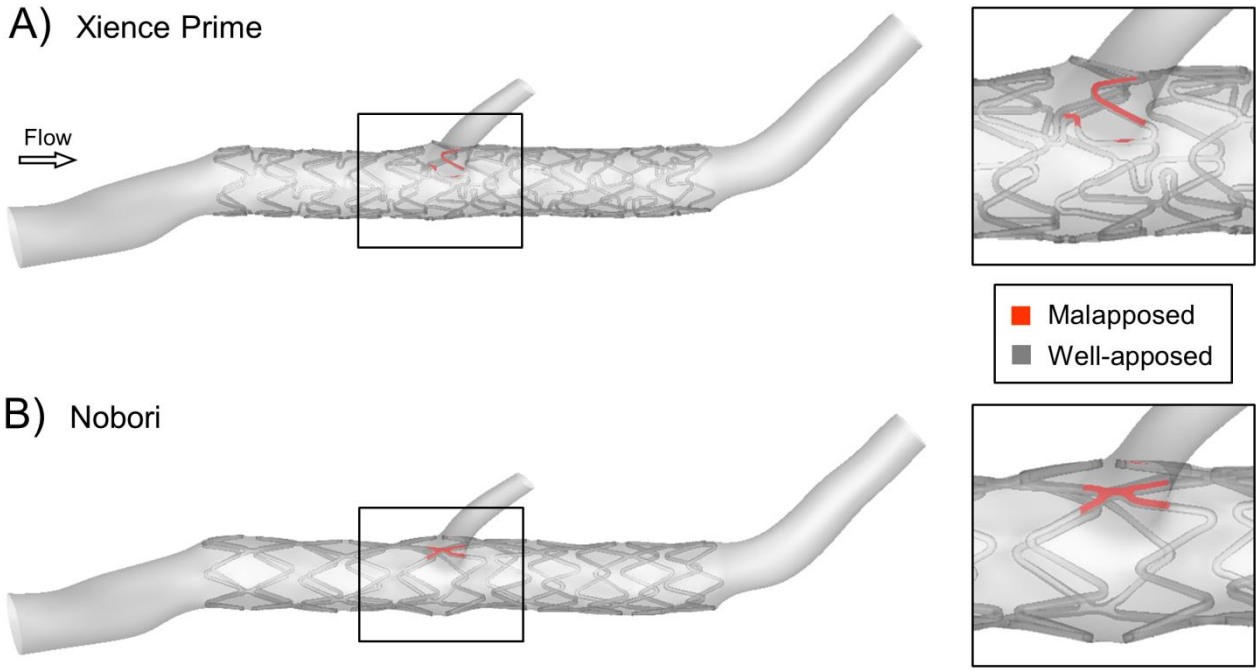

Figure 5 – Quantification of stent malapposition for Case 1: A) Xience Prime stent; B) Nobori stent. Malapposed struts are shown in red.

Post-print ve

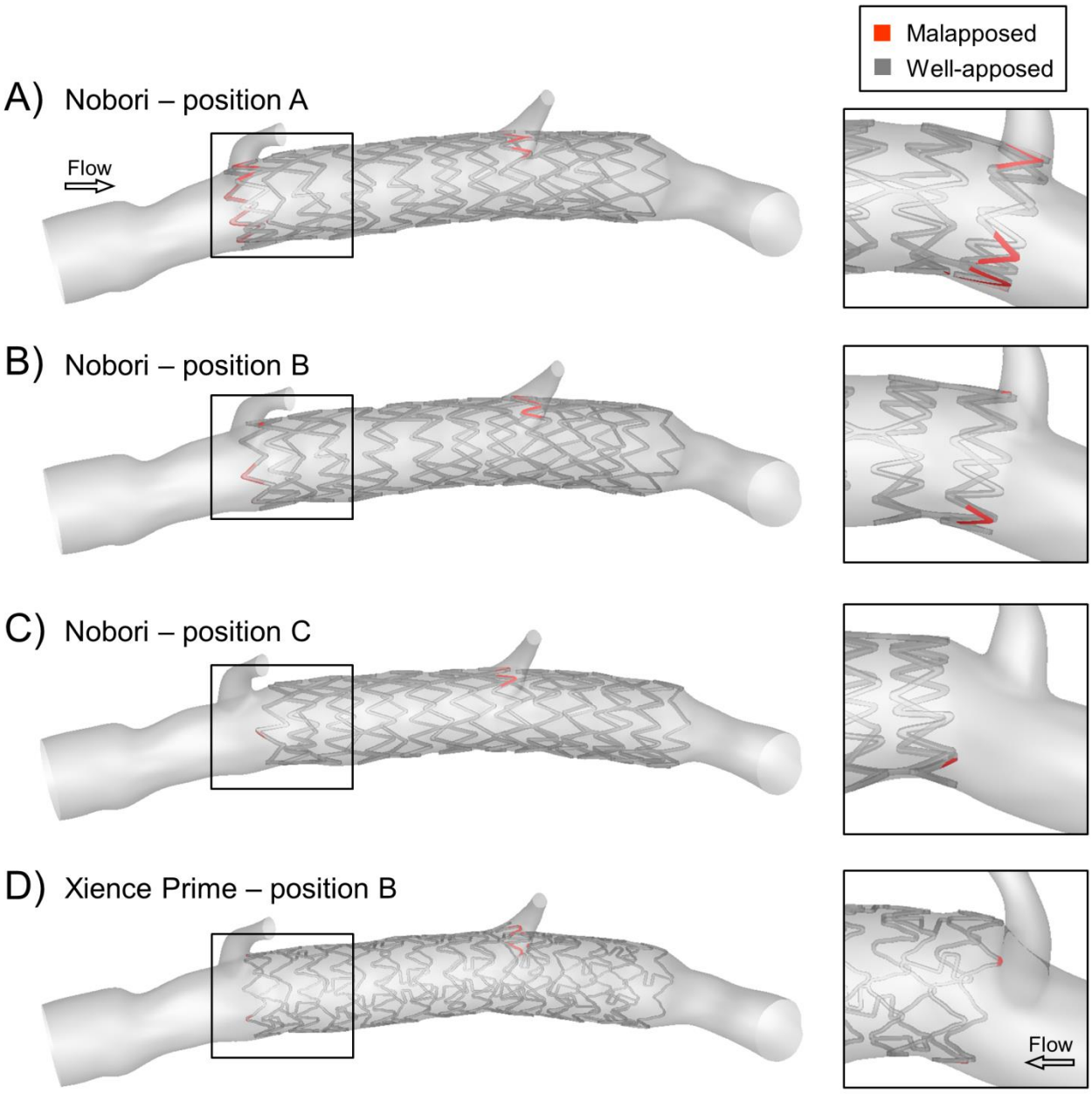

Figure 6 – Quantification of stent malapposition for Case 2. A-C) Nobori stent in the three positions investigated; D) Xience Prime stent. Malapposed struts are shown in red.

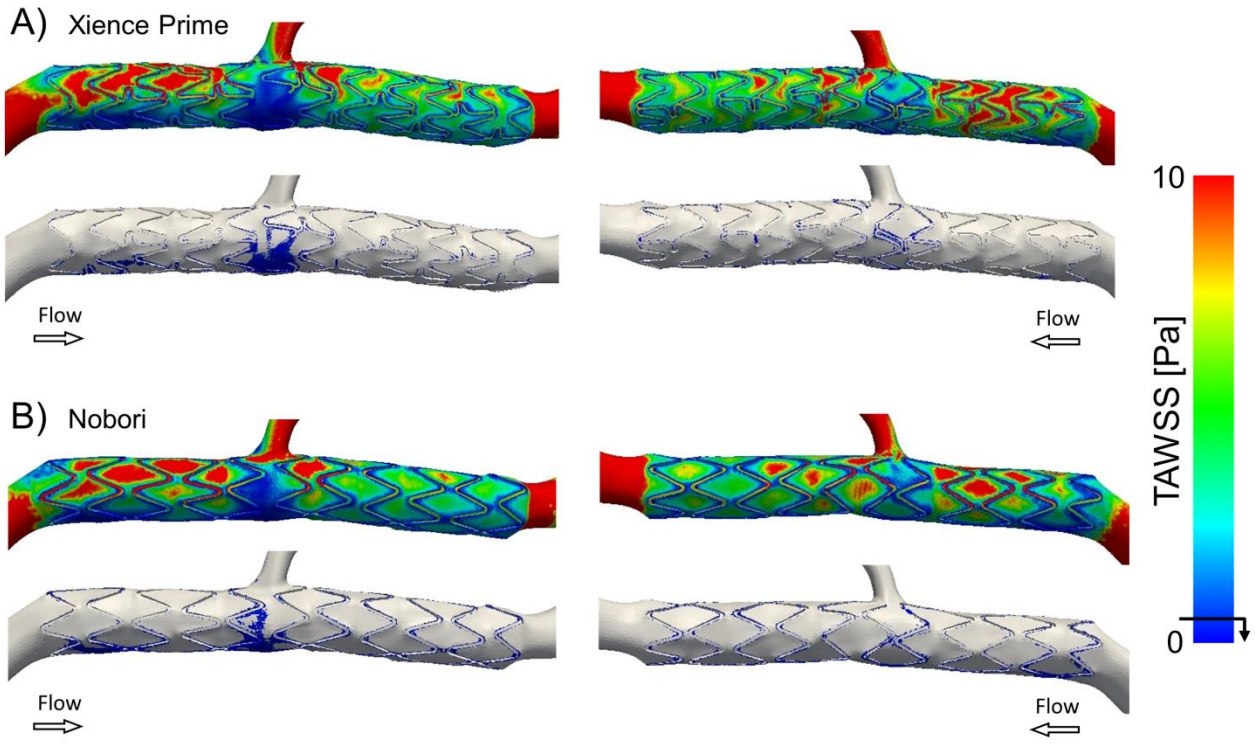

Figure 7 – Time-averaged wall shear stress (TAWSS) distributions for Case 1. Differences in TAWSS previously linked to neointimal thickness are shown in the figure and quantified in Table 2 by comparing CFD results from the implanted Xience Prime stent (A) vs the virtually-implanted Nobori stent (B). Two views are shown for clarity as indicated by differences in the flow direction in the left vs right images. The full range of TAWSS values is shown for both stents in each view. The lumen area exposed to the TAWSS < 0.4 Pa (see legend) is also isolated for both stents in each view.

Post-print v

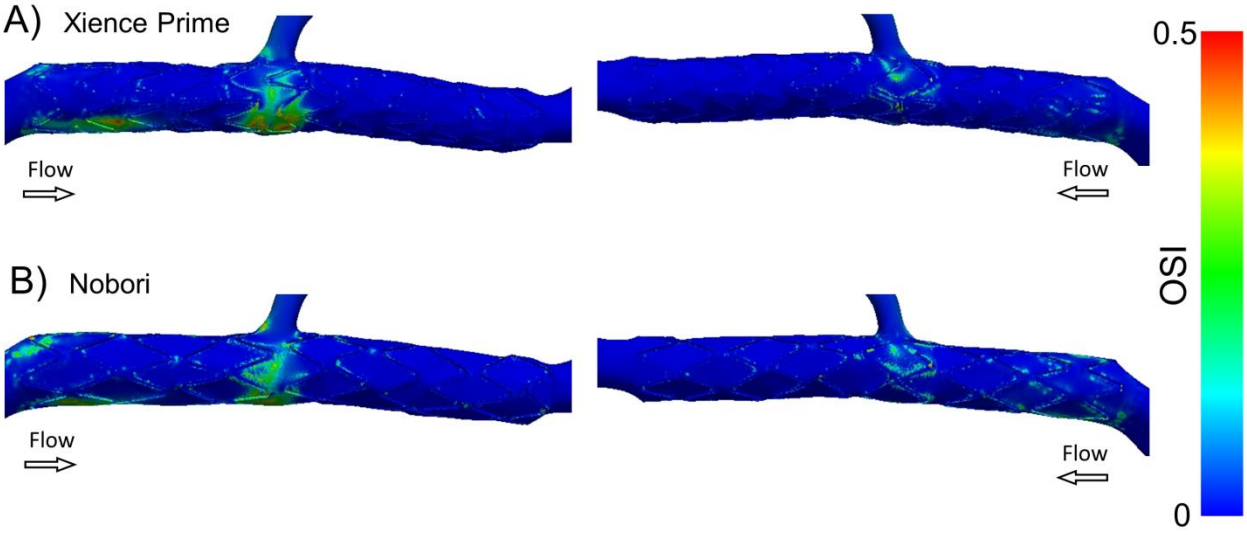

Figure 8 – Oscillatory shear index (OSI) distributions for Case 1. Differences in OSI are shown in the figure and quantified in Table 2 by comparing CFD results from the implanted Xience Prime stent (A) vs the virtually-implanted Nobori stent (B). Two views are shown for clarity as indicated by differences in the flow direction in the left vs right images.

Post-print vers

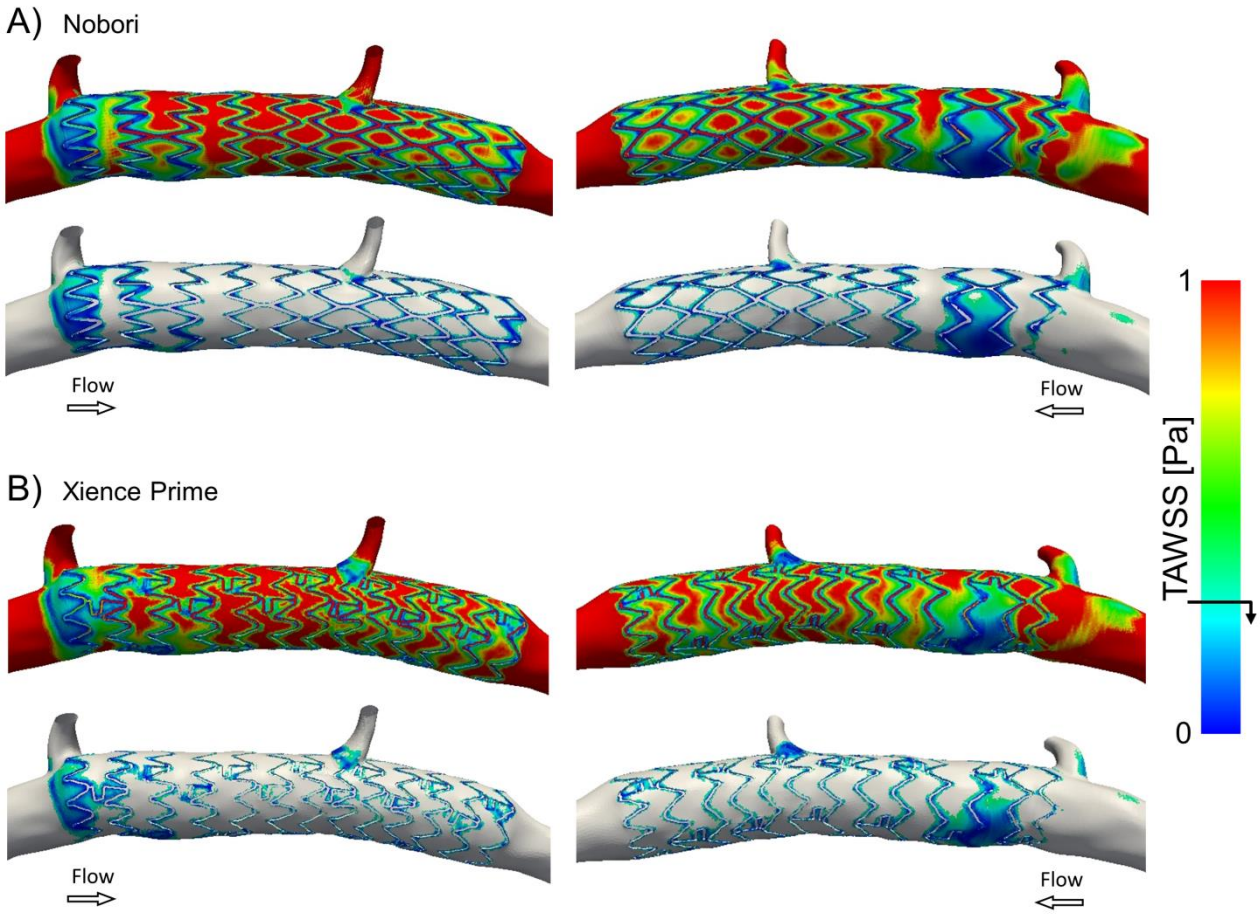

Figure 9 – Time-Averaged Wall Shear Stress (TAWSS) distributions for Case 2. Differences in TAWSS previously linked to neointimal thickness are shown in the figure and quantified in Table 2 by comparing CFD results from the implanted Nobori stent (A) vs the virtually-implanted Xience Prime stent (B). Two views are shown for clarity as indicated by differences in the flow direction in the left vs right images. The full range of TAWSS values is shown for both stents in each view. The lumen area exposed to the TAWSS < 0.4 Pa (see legend) is also isolated for both stents in each view.

Post-print

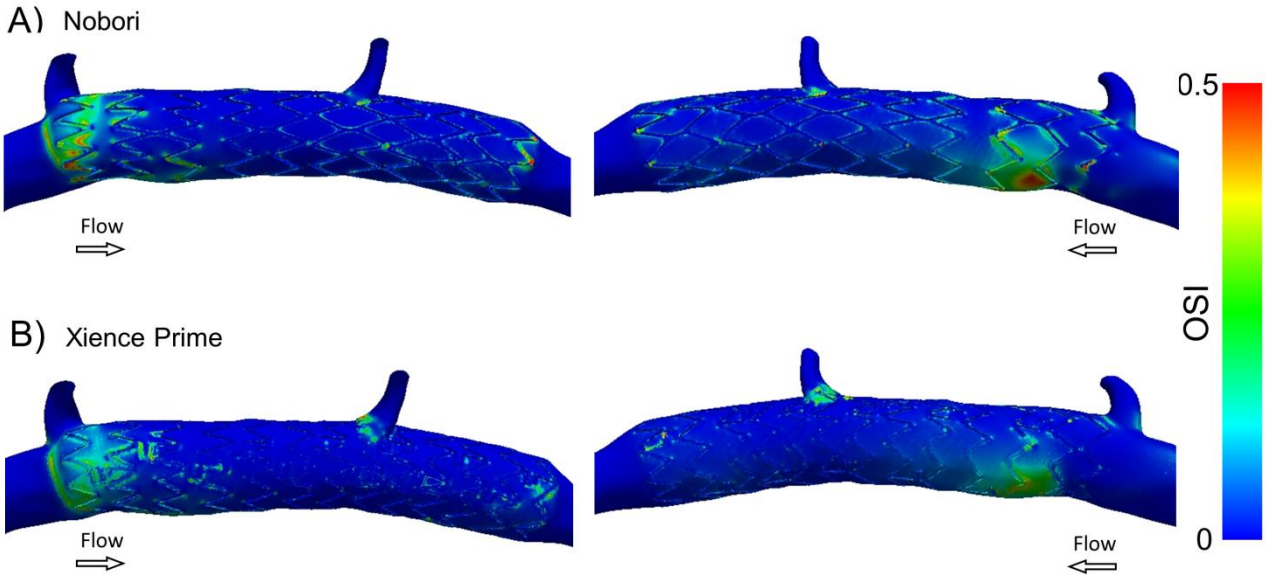

Figure 10 – Oscillatory Shear Index (OSI) distributions for Case 2. Differences in OSI are shown in the figure and quantified in Table 2 by comparing CFD results from the implanted Nobori stent (A) vs the virtually-implanted Xience Prime stent (B). Two views are shown for clarity as indicated by differences in the flow direction in the left vs right images.

Post-print vers